energies

Article

Seismic Monitoring at the Farnsworth CO₂-EOR Field Using Time-Lapse Elastic-Waveform Inversion of 3D-3C VSP Data

Xuejian Liu [1,*][ID], Lianjie Huang [1,*], Kai Gao [1], Tom Bratton [2][ID], George El-Kaseeh [3], William Ampomah [3], Robert Will [3], Paige Czoski [3], Martha Cather [3], Robert Balch [3] and Brian McPherson [4]

1   Los Alamos National Laboratory, MS D452, Los Alamos, NM 87545, USA; kaigao@lanl.gov
2   Tom Bratton LLC, 7 Mountain Oak, Littleton, CO 80127, USA; tom@tombrattonllc.com
3   New Mexico Tech, Petroleum Recovery Research Center, 801 Leroy Place, Socorro, NM 87801, USA;
    george.el-kaseeh@nmt.edu (G.E.-K.); william.ampomah@nmt.edu (W.A.); robert.will@nmt.edu (R.W.);
    paigeczoski@gmail.com (P.C.); martha.cather@nmt.edu (M.C.); robert.balch@nmt.edu (R.B.)
4   Department of Civil and Environmental Engineering, University of Utah, Salt Lake City, UT 84112, USA;
    b.j.mcpherson@utah.edu
*   Correspondence: xuejianliu17@gmail.com (X.L.); ljh@lanl.gov (L.H.)

Abstract: During the Development Phase of the U.S. Southwest Regional Partnership on Carbon Sequestration, supercritical CO₂ was continuously injected into the deep oil-bearing Morrow B formation of the Farnsworth Unit in Texas for Enhanced Oil Recovery (EOR). The project injected approximately 94 kilotons of CO₂ to study geologic carbon storage during CO₂-EOR. A three-dimensional (3D) surface seismic dataset was acquired in 2013 to characterize the subsurface structures of the Farnsworth site. Following this data acquisition, the baseline and three time-lapse three-dimensional three-component (3D-3C) vertical seismic profiling (VSP) data were acquired at a narrower surface area surrounding the CO₂ injection and oil/gas production wells between 2014 and 2017 for monitoring CO₂ injection and migration. With these VSP datasets, we inverted for subsurface velocity models to quantitatively monitor the CO₂ plume within the Morrow B formation. We first built 1D initial P-wave (V_p) and S-wave (V_s) velocity models by upscaling the sonic logs. We improved the deep region of the V_p and V_s models by incorporating the deep part of a migration velocity model derived from the 3D surface seismic data. We improved the shallow region of 3D V_p and V_s models using 3D traveltime tomography of first arrivals of VSP downgoing waves. We further improved the 3D baseline velocity models using elastic-waveform inversion (EWI) of the 3D baseline VSP upgoing data. Our advanced EWI method employs alternative tomographic and conventional gradients and total-variation-based regularization to ensure the high-fidelity updates of the 3D baseline V_p and V_s models. We then sequentially applied our 3D EWI method to the three time-lapse datasets to invert for spatiotemporal changes of V_p and V_s in the reservoir. Our inversion results reveal the volumetric changes of the time-lapse V_p and V_s models and show the evolution of the CO₂ plume from the CO₂ injection well to the oil/gas production wells.

Keywords: CO₂ monitoring; elastic-waveform inversion; enhanced oil recovery; Farnsworth; geologic carbon storage; time-lapse seismic monitoring; vertical seismic profiling (VSP)

1. Introduction

Time-lapse seismic data contain information about subsurface reservoir changes and can be inverted for reservoir imaging and monitoring [1]. Time-lapse seismic surveys have been widely used for monitoring geologic carbon storage [2]. Various time-lapse inversion methods have been developed during the last decade (e.g., [3–5]).

Because of the advantages of full-waveform inversion (FWI) that uses the complete information of seismic waveforms to invert for high-resolution distributions of subsurface elastic parameters [6], time-lapse FWI (TLFWI) or time-lapse EWI (TLEWI) have been used

for time-lapse seismic monitoring [5,7–10]. The velocity changes are inverted using time-lapse FWI in a two-step procedure: (1) construct the baseline velocity models, then (2) invert for the time-lapse changes of velocity models. Generally, there are two effective strategies for the implementation of the second step [7]: (1) sequential inversion, and (2) double-difference inversion. The latter strategy has a theoretically better performance, obtained by removing the negative influence of not matched baseline data [7,8], and [11]; however, it is less robust as it requires that time-lapse seismic data have excellent repeatability between surveys [10].

Despite this, most TLFWI experiments still utilize acoustic assumption because of the limit of computational capability. As the Earth is elastic, the acoustic assumption potentially results in incorrect estimations of subsurface models [8]. Elastic-waveform inversion can more accurately determine underground geophysical properties when compared with acoustic-waveform inversion [6]. With the exponential increase of computing power, it is becoming practical to implement elastic TLFWI [8]. However, previous studies were limited to synthetic data.

We apply 3D elastic TLEWI to time-lapse 3D VSP data acquired at the Farnsworth unit, Texas (Figure 1) to invert for spatiotemporal changes of seismic velocities during CO_2 injection [12] and migration. To our knowledge, this is the first application of TLEWI to time-lapse 3D field data. Before the time-lapse VSP surveys, a 3D surface seismic dataset was acquired in 2013 that covered a wide area at the Farnsworth unit for site characterization [13]. Next, a 3D baseline VSP dataset was acquired in 2014 before CO_2 injection. Each common-shot VSP dataset contains three components (3C), X (East), Y (North), and Z (Vertical), and can be separated as downgoing and upgoing wavefields, as displayed in Figure 2.
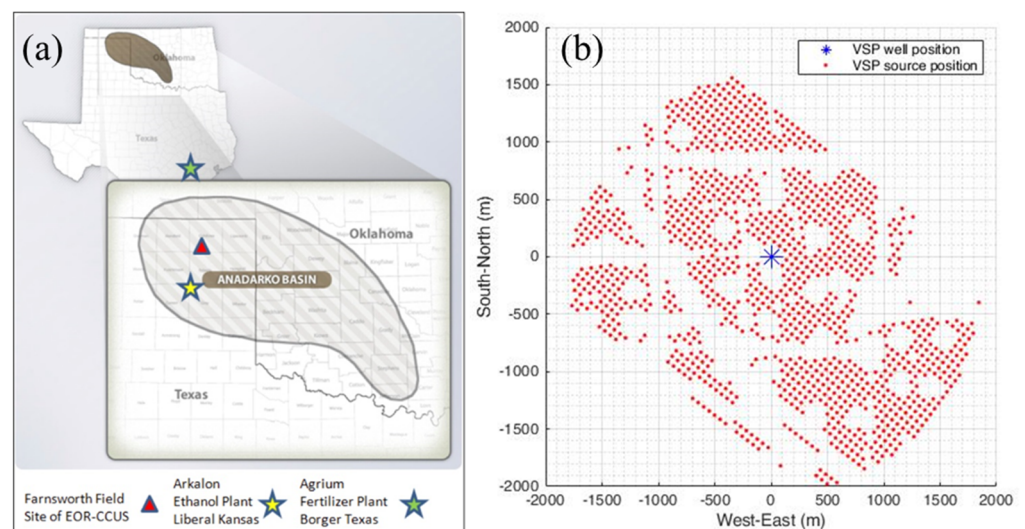

Figure 1. (**a**) Location of the Farnsworth CO_2-EOR field as indicated by the red up-pointing triangle, and (**b**) VSP acquisition geometry for the baseline 3D-3C VSP survey.

Subsequently, tons of anthropogenic CO_2 were continuously injected to drive subsurface fluids containing oil and gas into production wells. To monitor the development of the CO_2 plume, three repeat 3D-3C VSP datasets were acquired in 2015, 2016, and 2017. Compared to the surface seismic survey, VSP has the following advantages: (1) it allows more convenient time-lapse acquisition with fixed 3C geophones in a well, and (2) VSP data contain fewer noises and are free of contaminations of surface waves. Additionally, compared to cross-well seismic monitoring [4], VSP surveys provide broader subsurface monitoring. However, the VSP downgoing free-surface multiples are strong events and can cover most late arrivals after the first-arrival P-waves [14]; this can also be observed from Figure 2a. By contrast, the VSP upgoing free-surface multiples are much weaker and located at later time; therefore, their negative effects for velocity inversion can be

neglected by using a time window for inversion. We use the separated upgoing waves for EWI to update the deep region of the 3D baseline V_p and V_s models and for TLEWI of the time-lapse 3D VSP data.
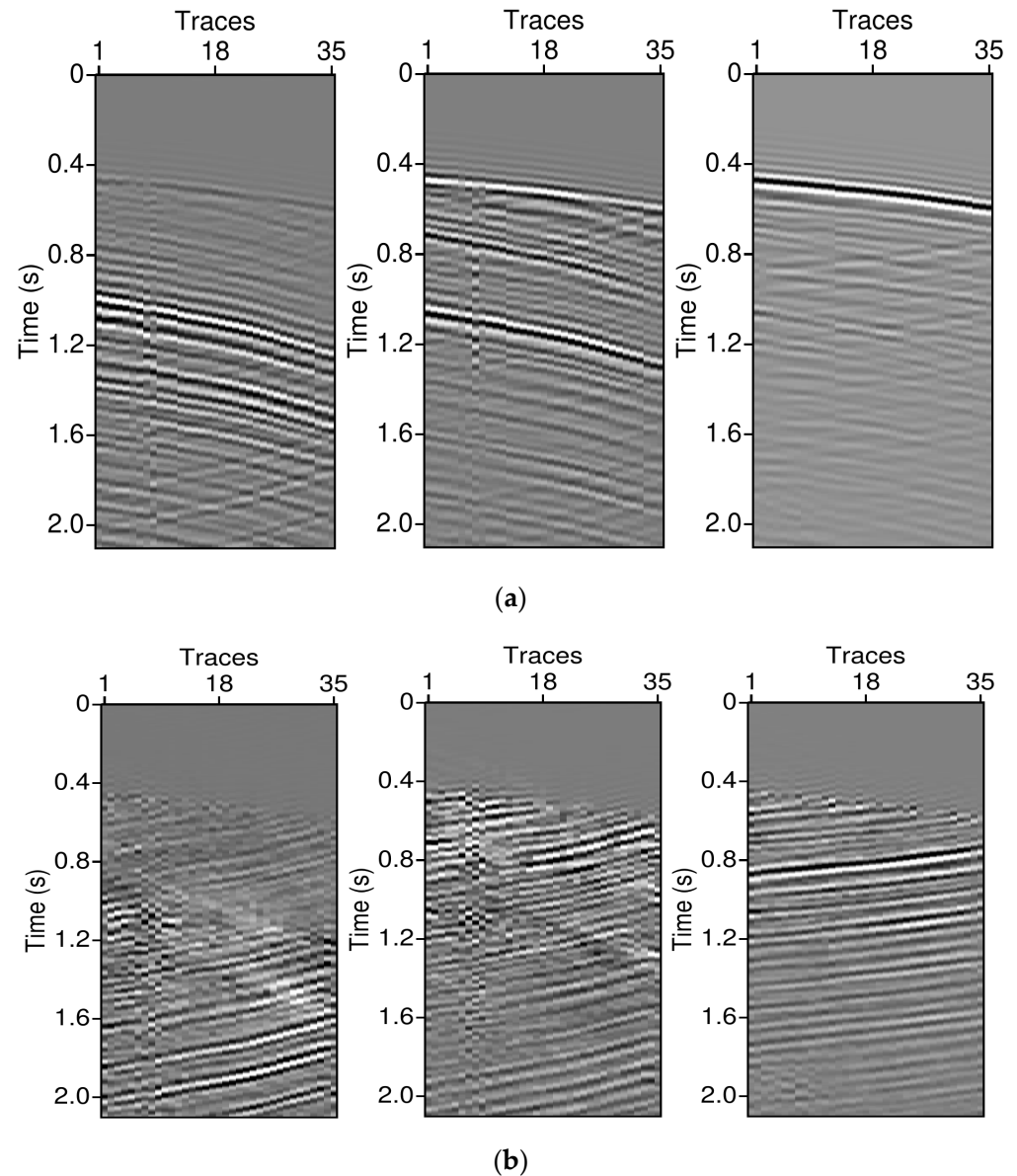

Figure 2. Left, middle, and right panels show X (East), Y (North) and Z (Vertical) components, respectively, of (**a**) full wavefield data and (**b**) the separated upgoing data of the baseline 3D-3C VSP survey.

We organize the paper as follows. We first present the practical workflow for 3D V_p and V_s inversion, and then apply our workflow to the baseline 3D VSP data and three time-lapse monitoring 3D VSP data. Our results reveal the volumetric evolution of time-lapse velocity changes with the increasing injection of CO_2.

2. Method

First, we pre-process the baseline and monitoring surveys of 3D-3C VSP seismic datasets using the following consistent workflow: first break picking, 3C geophone orientation, noise attenuation, surface consistent amplitude compensation, and wavefield separation for downgoing and upgoing data. The processing datum is at approximately

945 m (3100 feet) above sea surface. The processed VSP data, as shown in Figure 2, contain 35 geophones within a depth range between 1140 m and 1688 m.

Then, we introduce a workflow including waveform inversion to build the baseline velocity models. Next, we perform the sequential waveform inversions of cross-equalized monitoring data to obtain time-lapse velocity models. We obtain time-lapse velocity changes by subtracting the baseline velocity model from time-lapse velocity models. The procedure is generally summarized in Figure 3.
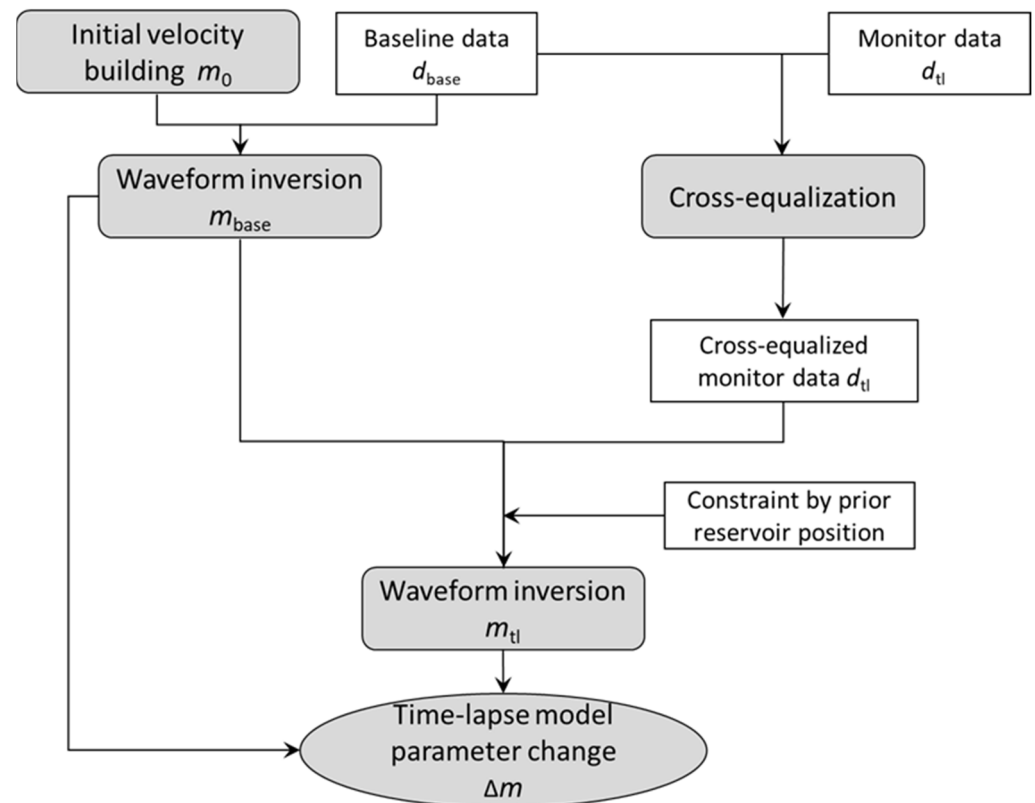

Figure 3. Workflow of time-lapse seismic processing and inversion for time-lapse velocity changes.

2.1. Building the Baseline Velocity Models

We build the initial V_p and V_s models by combining information from the sonic logs, the 3D surface seismic survey, and the baseline 3D VSP survey. First, we upscale the sonic logs using the Schoenberg–Muir method [15] within layers divided according to P-wave impedance. We compute the 1D initial V_p and V_s models (Figure 4) using the upscaled elastic moduli and densities.

Beneath the maximum depth of the sonic logs, we improve the initial V_p velocity model by appending the inverted velocities from Schlumberger's state of the art reflection tomography of the 3D surface seismic data. As the surface seismic survey covers a much larger surface area than the VSP survey, some reflection events with large-reflection angles are recorded by surface seismic data. Reflection tomography of surface seismic data [16] provides long-wavelength velocity updates for the deep subsurface. We update the initial V_s velocity model in the deep region according to the V_p/V_s ratio at the lower boundary of the sonic log (Figure 5).
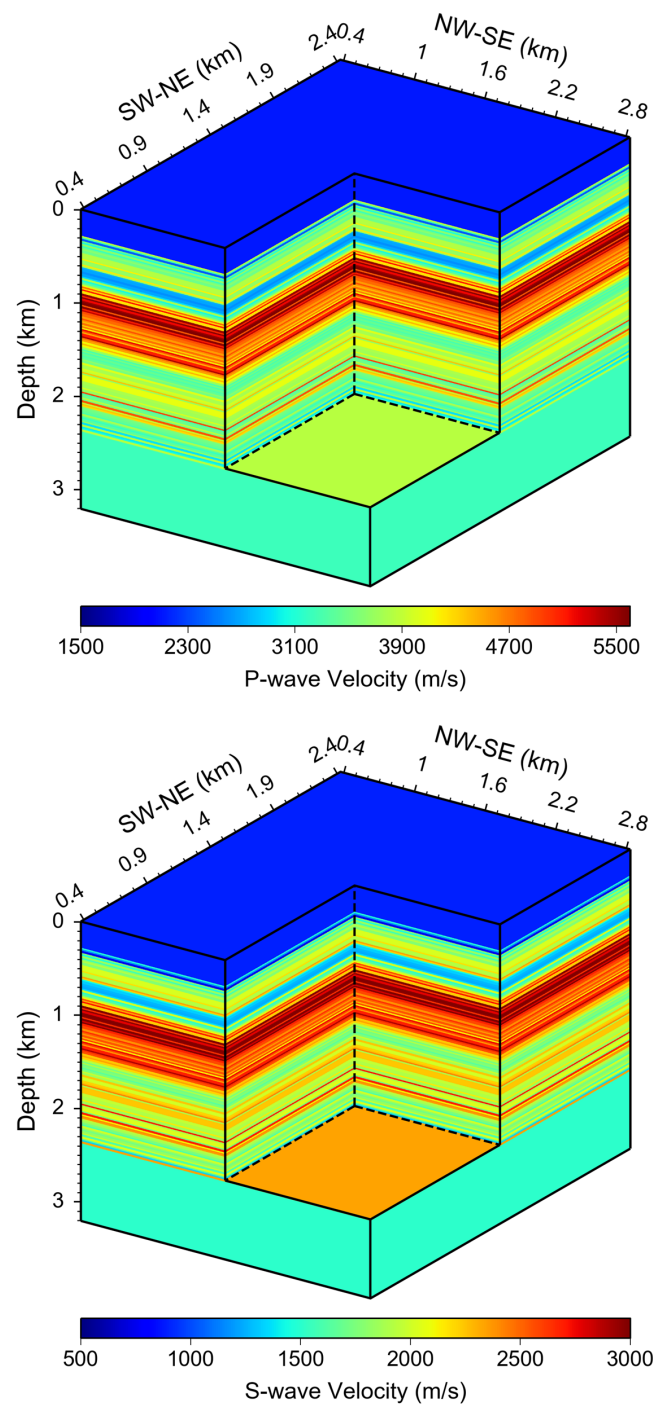
Figure 4. Initial baseline P-wave (V_p) and S-wave (V_s) velocity models obtained by upscaling the sonic log.

Above the well head of logging, we improve the initial V_p velocity model using tomography of picked first-arrivals:

$$f(V_p) = \frac{1}{2} \int \int \left(t_{cal}(V_p) - T_{obs} \right)^2 d\mathbf{x}_r d\mathbf{x}_s, \tag{1}$$

where t_{cal} is the computed traveltime using the updated V_p model, and T_{obs} is the observed first-arrival traveltime. We employ adjoint-state first-arrival traveltime tomography (FATT) [17]; this calculates the velocity gradient using the adjoint-state method and is more suitable for 3D velocity building with much reduced memory-storage requirement when

compared to classic traveltime tomography. We update the shallow region of the V_s velocity model using the FATT V_p updates according to the V_p/V_s ratios at the upper boundary of the sonic logs (Figure 6).
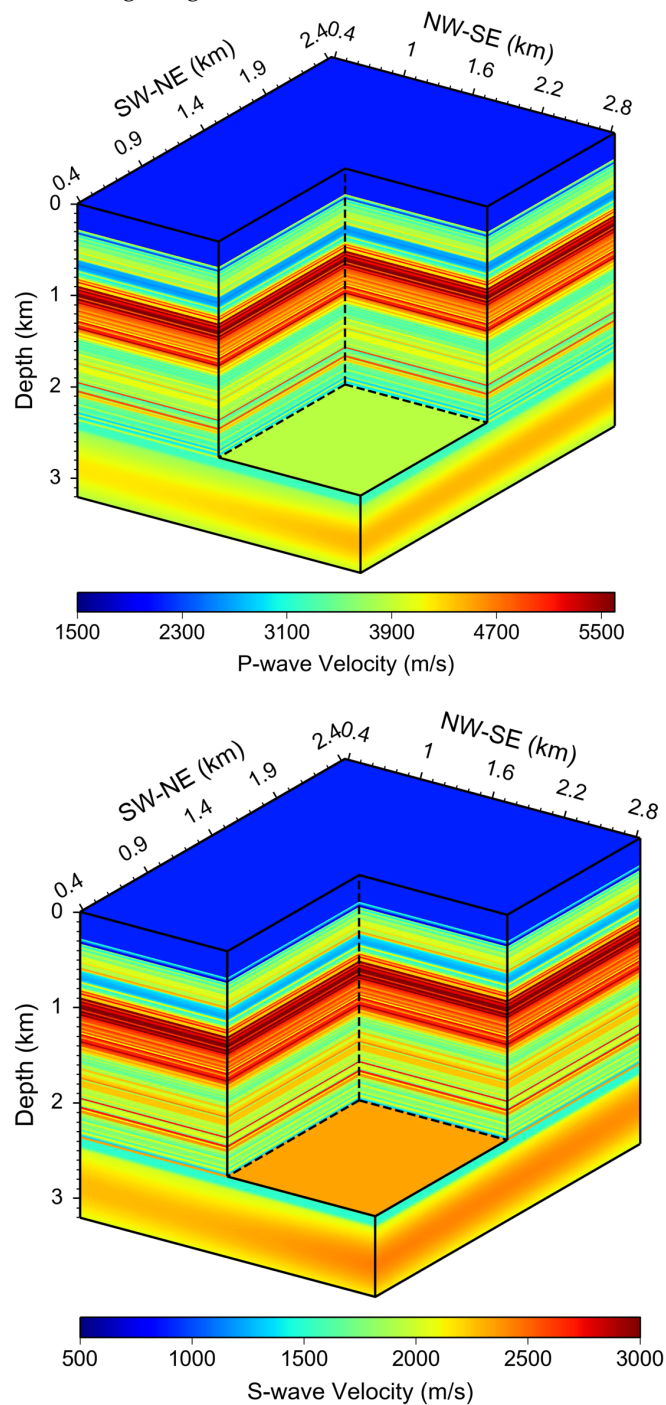

Figure 5. Updated baseline V_p model by incorporating the deep region of the velocity model derived from the 3D surface seismic data and V_s model with the deep region updated according to the V_p/V_s ratio at the lower boundary of the sonic logs.
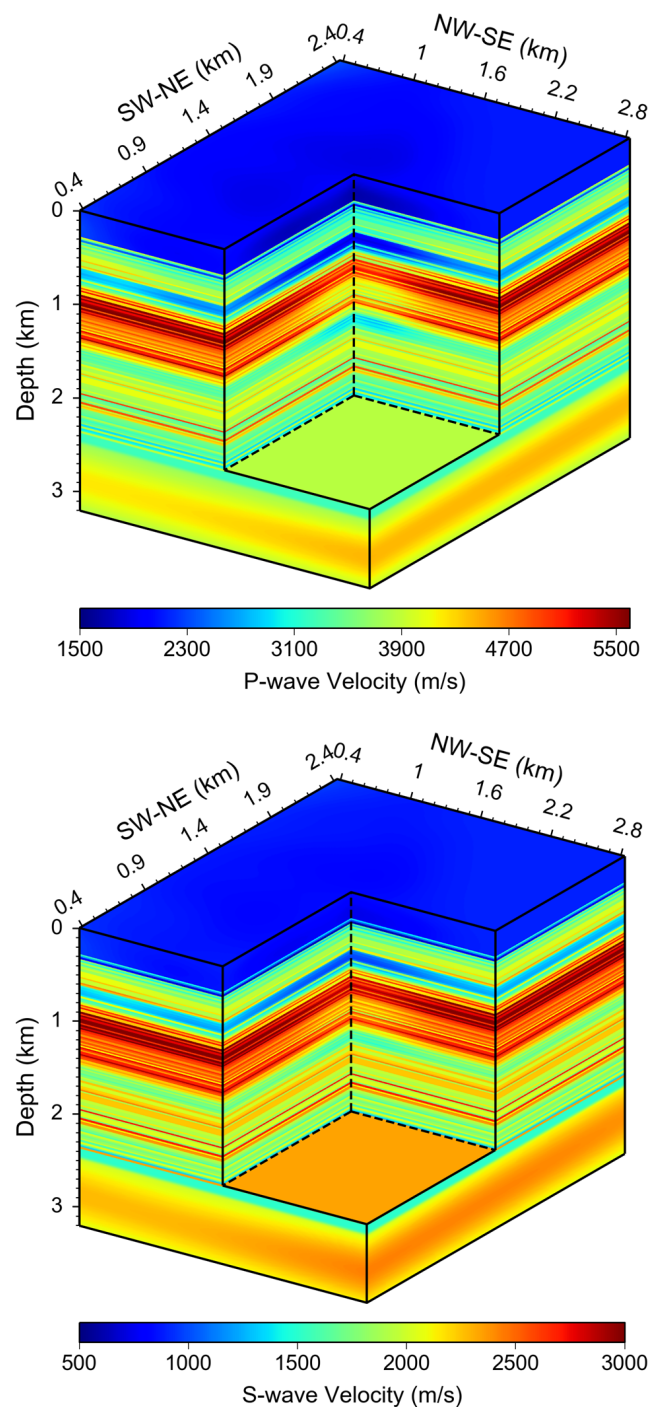
Figure 6. Improving the shallow regions of the baseline V_p model using first-arrival tomography of the downgoing waves of the baseline VSP data, together with V_s model with estimated updates for the shallow region according to the V_p/V_s ratios at the upper boundary of the sonic logs.

2.2. Elastic-Waveform Inversion of 3D-3C VSP Data

We use EWI of 3C VSP upgoing data, as shown in Figure 2b, to improve V_p and V_s models with both tomographic parts and high-resolution details, especially for the deep region beneath the reservoir.

For EWI implementation, the conventional L_2-norm-based misfit measures differences between observed and synthetic seismic data with both amplitudes and phases. However, there usually exist unreliable amplitudes in seismic data due to unknown source/receiver coupling and seismic processing procedures without preserving amplitudes as well as

unknown exact subsurface physics (e.g., density and attenuation are not fully considered in forward modeling for synthetic data). All the above issues can make the L_2-norm-based misfit fail to converge. In our EWI, we employ a cross-correlation-based misfit [18]:

$$f(\mathbf{m}) = \int \int \left(1 - \frac{\int \mathbf{d}_m(\mathbf{x}_r, t; \mathbf{x}_s)\mathbf{d}_{obs}(\mathbf{x}_r, t; \mathbf{x}_s)dt}{\sqrt{\int \mathbf{d}_m^2(\mathbf{x}_r, t; \mathbf{x}_s)dt}\sqrt{\int \mathbf{d}_{obs}^2(\mathbf{x}_r, t; \mathbf{x}_s)dt}} \right) d\mathbf{x}_r d\mathbf{x}_s, \tag{2}$$

which measures the global phase closeness between the synthetic data $\mathbf{d}_m$ and the observed seismic data $\mathbf{d}_{obs}$. In Equation (2), t, $\mathbf{x}_r$, $\mathbf{x}_s$, and $\mathbf{m}$ represent recording time, receiver position, source position, and the models including V_p and V_s to be inverted, respectively. The gradient in EWI inversion is computed using the adjoint-state method to the first-order velocity-stress elastic-wave equations as follows:

$$\frac{\partial f}{\partial \lambda} = -\int \int \left(\frac{\partial v_x}{\partial x} + \frac{\partial v_y}{\partial y} + \frac{\partial v_z}{\partial z} \right) \left(\frac{\partial \widetilde{u}_x}{\partial x} + \frac{\partial \widetilde{u}_y}{\partial y} + \frac{\partial \widetilde{u}_z}{\partial z} \right) dt d\mathbf{x}_s,$$

$$\frac{\partial f}{\partial \mu} = -\int \int \begin{pmatrix} \left(\frac{\partial v_x}{\partial z} + \frac{\partial v_z}{\partial x} \right)\left(\frac{\partial \widetilde{u}_x}{\partial z} + \frac{\partial \widetilde{u}_z}{\partial x} \right) + \\ \left(\frac{\partial v_x}{\partial y} + \frac{\partial v_y}{\partial x} \right)\left(\frac{\partial \widetilde{u}_x}{\partial y} + \frac{\partial \widetilde{u}_y}{\partial x} \right) + \\ \left(\frac{\partial v_y}{\partial z} + \frac{\partial v_z}{\partial y} \right)\left(\frac{\partial \widetilde{u}_y}{\partial z} + \frac{\partial \widetilde{u}_z}{\partial y} \right) + \\ 2\left(\frac{\partial v_x}{\partial x}\frac{\partial \widetilde{u}_x}{\partial x} + \frac{\partial v_y}{\partial y}\frac{\partial \widetilde{u}_y}{\partial y} + \frac{\partial v_z}{\partial z}\frac{\partial \widetilde{u}_z}{\partial z} \right) \end{pmatrix} dt d\mathbf{x}_s, \tag{3a}$$

where λ and μ are Lamé moduli, (v_x, v_y, v_z) represents particle velocity components of source wavefields, and $(\widetilde{u}_x, \widetilde{u}_y, \widetilde{u}_z)$ represents the displacement components of adjoint receiver wavefields. To reduce inter-parameter cross-talks, we further rewrite gradients with respect to V_p and V_s as

$$\begin{aligned} \frac{\partial f}{\partial v_p} &= \frac{\partial f}{\partial \lambda}\frac{\partial \lambda}{\partial v_p} = 2\rho_0 v_p \frac{\partial f}{\partial \lambda}, \\ \frac{\partial f}{\partial v_s} &= \frac{\partial f}{\partial \lambda}\frac{\partial \lambda}{\partial v_s} + \frac{\partial f}{\partial \mu}\frac{\partial \mu}{\partial v_s} \\ &= -4\rho_0 v_s \frac{\partial f}{\partial \lambda} + 2\rho_0 v_s \frac{\partial f}{\partial \mu}. \end{aligned} \tag{3b}$$

We first improve the entire models along seismic wavepaths (tomographic updates) and then invert for high-resolution details of the models, particularly in the region beneath the reservoir (conventional updates). We extract tomographic parts or keep the conventional format of gradient G with the operation [19,20] as

$$G_{tomo/conventional} = W_s W_r + \alpha H_z(W_s)H_z(W_r), \tag{4}$$

where imaging-condition weighting coefficient $\alpha = 1 \ or \ 0$ produces tomographic or conventional kernel, respectively, H_z represents the Hilbert transform along the depth direction, and W_s and W_r denote any combination pair of source and adjoint wavefield components in Equation (3), which are applied to all the combination pairs.

Furthermore, during the inversion, we use an alternating Tikhonov and total-variation (TV) regularization schemes to penalize possible inversion noise [21]:

$$\mathbf{m}^{(i)} = \underset{\mathbf{m}}{\text{argmin}}\left\{ f(\mathbf{m}) + \frac{\varepsilon_1}{2}\left\| \mathbf{m} - \mathbf{u}^{(i-1)} \right\|_2^2 \right\}, \tag{5a}$$

and

$$\mathbf{u}^{(i)} = \underset{\mathbf{u}}{\text{argmin}}\left\{ \frac{\varepsilon_1}{2\varepsilon_2}\left\| \mathbf{m}^{(i)} - \mathbf{u} \right\|_2^2 + \left\| \mathbf{u} \right\|_{TV} \right\}, \tag{5b}$$

where the superscript i represents the iteration number, $\mathbf{u}$ denotes TV de-noised auxiliary models with an initial guess of $\mathbf{u}^{(0)} = \mathbf{m}^{(0)}$, and ε_1 and ε_2 are regularization weighting coefficients. The TV-denoised auxiliary term serves as the prior model in the Tikhonov regularization term, which removes noise and stabilizes the inversion procedure. We

employ generalized TV de-noising by incorporating a second-order derivative term in Equation (5b); this produces more reliable results than conventional TV-de-noising/ regularization that assumes piece-wise constant [21].

2.3. Time-Lapse Inversion Strategies

With the updated baseline V_p and V_s models obtained using EWI of baseline upgoing VSP data, we can use a sequential method or a double-difference method to invert for time-lapse velocity changes [7]. The time-lapse 3D VSP data contain several inconsistent source positions, and the inconsistency increases for the data acquired later. Thus, the repeatability of seismic data becomes worse for the VSP data acquired later. Additionally, the double-difference method requires an additional processing step during which the time-lapse difference of observed data are summed together with the synthesized data modeled with inverted baseline velocity models; this can be challenging if the amplitudes of synthetic data do not match well with those of the field data. Therefore, we use the sequential inversion strategy to obtain the time-lapse velocity changes due to its lower repeatability requirement during inversion of time-lapse VSP data.

We implement the sequential strategy in our EWI of time-lapse 3D-3C VSP data using 3D EWI-updated baseline V_p and V_s models as the initial models of TLEWI. The time-lapse changes resulting from the CO_2 injection and migration are expected to be bounded within a thin reservoir layer called Morrow B [22]. Such a change does not generate cycle-skipping effects in the frequency band of the inversion. We invert the upgoing data of the time-lapse VSP datasets using the frequency band used in EWI of the baseline VSP data. The misfit function in Equation (2) is solved for velocity models during monitoring stages. We obtain the time-lapse changes of seismic velocities by subtracting the baseline velocity models from the velocity models during the monitoring stages.

To obtain high-quality time-lapse inversion results, we employ cross-equalization [23] to balance the VSP data between the baseline survey and repeat surveys (see the workflow in Figure 3) within the time window of less than 1 s. This procedure is particularly useful when there exist waveform distortions between the datasets of the repeat surveys and that of the baseline survey, particularly the time-lapse distortions caused by the near surface weathering zone. Because the Morrow B reservoir formation is a thin layer that is challenging for EWI, we use a spatial mask enclosing the possible range of velocity changes as a spatial prior in EWI to increase the robustness of EWI and reduce inversion uncertainty.

3. Site Characterization

The Farnsworth CO_2-EOR field in Ochiltree, Texas (Figure 1a), is a site for a field demonstration of geologic carbon storage. The Farnsworth Unit (FWU) is the largest Morrowan oil field in the western part of the Anadarko Basin. The uppermost sandstone, "Morrow B," is the reservoir for CO_2-EOR. The thickness of the Morrow B formation ranges from 0 m to about 16.5 m (54 feet) [22].

One million tons of supercritical CO_2 produced from an Ethanol Plant and a Fertilizer Plant nearby was planned to be injected into the Morrow B formation. Well 13-10A was used for CO_2 injection and 3D-3C VSP data acquisition. Figure 1b shows seismic sources of the baseline VSP survey surrounding Well 13-10A. In the velocity models, the well is at the distance of 1403 m along South-West (SW)-North-East (NE) direction and at distance of 1642 m along North-West (NW)-South-East (SE) direction.

A baseline 3D-3C VSP dataset was acquired in November 2014 and then repeat 3D-3C VSP datasets were acquired in January 2015 (Monitor 1), November 2016 (Monitor 2), December 2017 (Monitor 3) for monitoring CO_2 injection and migration. A total of 33,070.25, 76,597.14, and 94,286.38 tons of CO_2 were injected from the baseline survey to the Monitor 1, Monitor 2, and Monitor 3 survey, respectively.

4. Results and Discussion

We built the baseline velocity models using the processed 3D-3C VSP data and the workflow as described in Figure 3. All models are discretized with a grid interval of 7.62 m (25 feet) along three axes. Figure 4 shows the initial V_p and V_s baseline velocity models built after upscaling the sonic logs. With the seismic datum as the zero-depth position, well recording started from the depth of 260.5 m (854.5 feet); seismic velocities V_p and V_s at this depth are extended to the entire shallower space. Figure 5 depicts the updated baseline velocity model after appending the deep region of the velocity model derived from the 3D surface seismic data. We then improved the shallow region of the baseline V_p model using 3D tomography of the first arrivals of the baseline VSP downgoing waves, as displayed in Figure 6. In Figures 5 and 6, we estimated updates for the initial V_s velocity model below and above the depth range of the sonic logs from V_p updates according to the V_p/V_s ratios at the lower and the upper boundaries of the sonic logs.

We improved the baseline velocity models using 3D elastic-waveform inversion of the baseline 3D-3C VSP upgoing data. We filtered the data with a maximum frequency of 30 Hz. We estimated the source wavelets by stacking the first-arrivals of vertical components. We performed multi-scale EWI of VSP upgoing data to improve the baseline velocity models using three bandpass frequency scales (3-5–9-12 Hz, 3-5–17-20 Hz, and 3-5–27-30 Hz). During inversion, ten iterations were used for each frequency band. A Gaussian smoother with a radius of two grid points was applied to the gradient to suppress possible noises, while maximum updates for V_p and V_s at each iteration were set as 100 m/s and 50 m/s to avoid abnormal velocity perturbations and make iterative updates satisfy linear properties, respectively. In addition, the generalized TV de-noising constraint was applied at the final frequency band to stabilize the inversion procedure, where the regularization damping parameter ε_1 (in Equation (5a)) was set as $0.2 \times \frac{\|\nabla f(\mathbf{m}^{(i)})\|}{\|\mathbf{m}^{(i)} - \mathbf{u}^{(i-1)}\|}$ and the regularization damping parameter $\frac{\varepsilon_1}{2\varepsilon_2}$ (in Equation (5b)) was set as 0.02 (refer to [21]). Figure 7 depicts the final updated baseline velocity models; Figure 8 displays the velocity updates. EWI of VSP upgoing data provides low-wavenumber tomographic update and high-resolution updates for the deep region of the baseline velocity models. The convergence curves shown in Figure 9 show robust convergence of velocity inversions at three frequency scales. More specifically, the frequency band of 3-5–17-20 Hz show the best convergence; the inversion in the lower-frequency band faces the challenge of lower signal-to-noise ratios and the inversion in the higher-frequency bands faces the challenge of high nonlinearities. In addition, as the input model in the third stage might have been close enough to the real model, the inversion convergence of the highest-frequency band data becomes much slower.

After obtaining the baseline velocity models, we performed TLWEI of the time-lapse 3D-3C VSP data to quantitatively measure time-lapse velocity changes that indicate evolution of the CO_2 plume. We computed the time-lapse velocity changes by subtracting the baseline velocity models from the sequentially inverted velocity models during the monitoring stages (using same inversion parameters as the baseline inversion). Figures 10–12 show the velocity changes between baseline and Monitor 1, Monitor 2, and Monitor 3 at the center depth of Morrow B, respectively. The increasing velocity reductions correspond to continuously increased CO_2 injection over several years. Additionally, time-lapse V_p changes show large values near the CO_2 injection well (the red star in those figures). The steadily dropping convergence curves in Figure 13 show the reliability of inverted time-lapse velocity changes, where larger convergence drops in the monitoring stages correspond well with larger time-lapse data differences and velocity reductions.
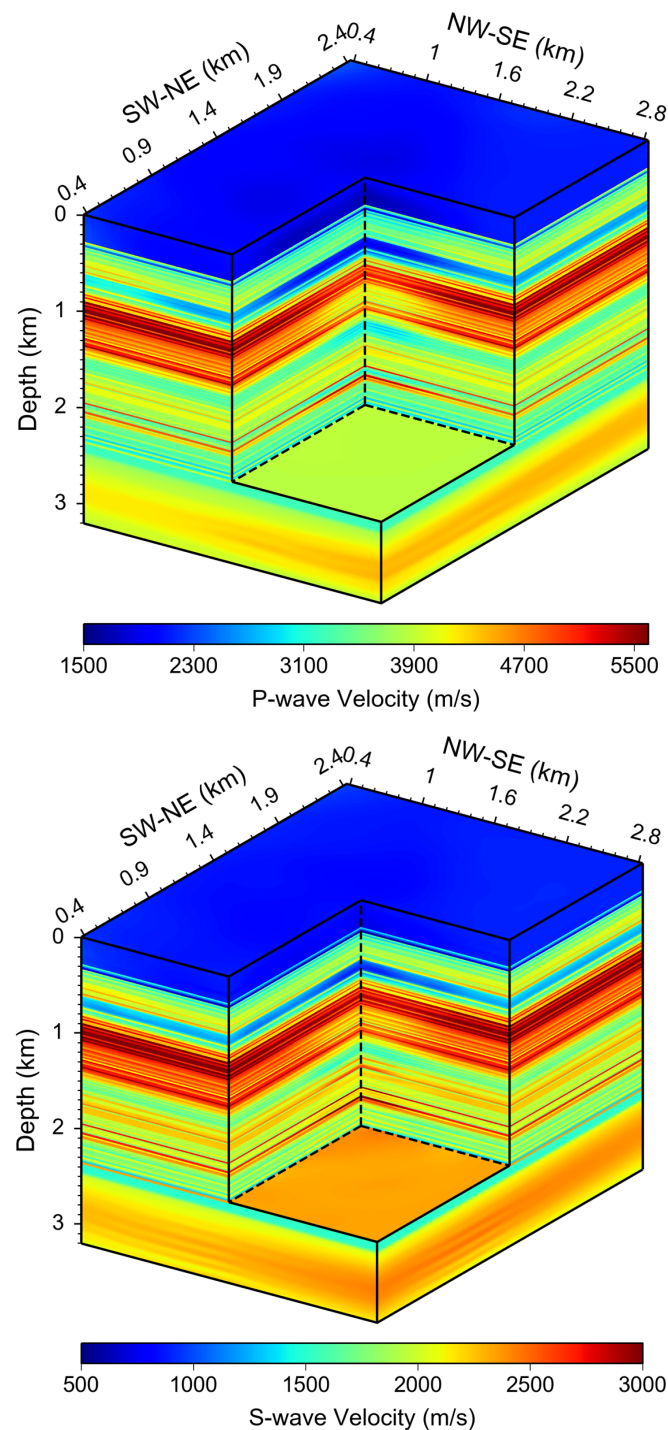
Figure 7. Final updated baseline velocity models obtained using 3D elastic-waveform inversion of 3C VSP upgoing waves of the baseline VSP data.

Figure 14 is a comparison of inversion results with the well logs. Note that the depths are measured with the reference of the well head, which is 16.2 m (53 feet) lower than the seismic processing datum. The maximum reduction in V_p in Monitor 3 occurs just above the Morrow B sand while the maximum reduction in V_s in Monitor 3 occurs well below the Morrow B sand. If there is slippage on a weak bedding plane below the Morrow B sand, it would reduce the horizontal stress below the sand. Because of the negligible fluid effect on the S-wave velocity, the reduction in shear-wave velocity occurs at a lower depth. The V_p is dependent on both changes in stress and fluids. Since carbon dioxide is more buoyant

than the water, it is expected to reduce the P-wave velocity at shallower depths. Note that the inverted time-lapse V_p and V_s changes for this CO_2-EOR field are significantly smaller than those of petrophysical prediction for CO_2 flooding [24].
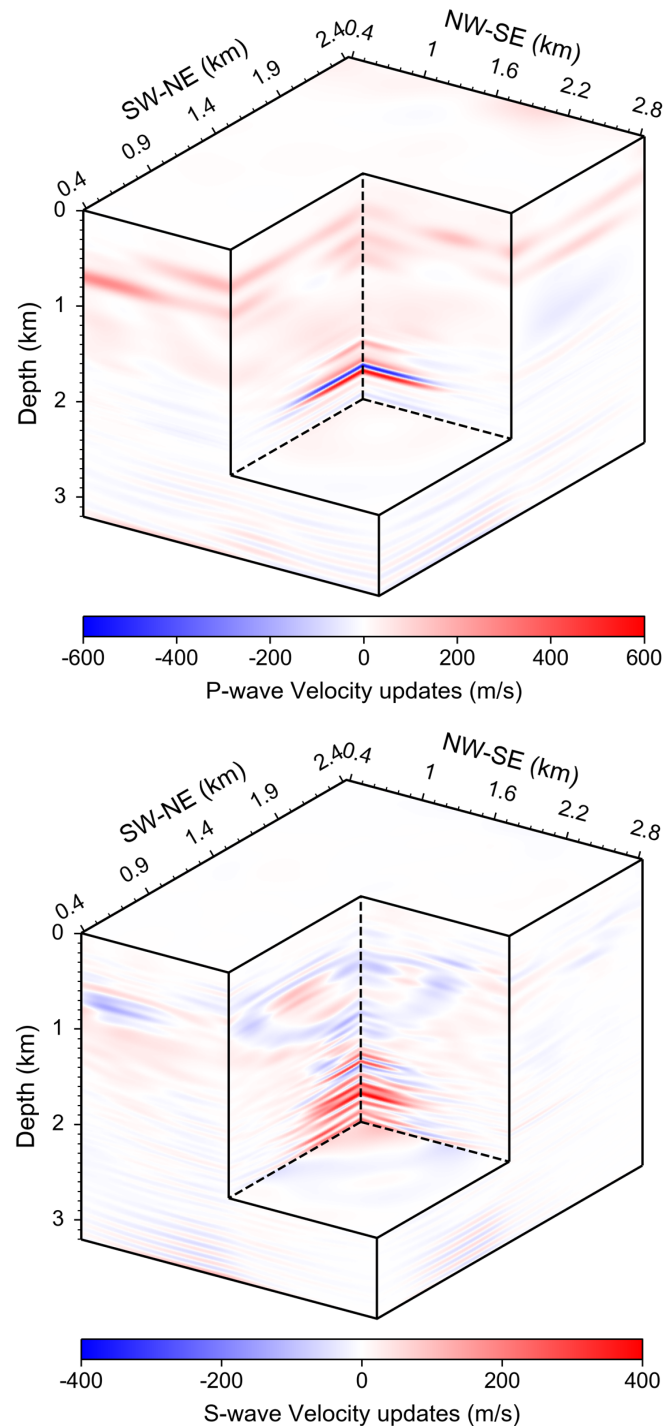
Figure 8. Velocity updates obtained using 3D elastic-waveform inversion of 3C VSP upgoing waves of the baseline VSP data (i.e., differences by subtracting models in Figure 6 from those in Figure 7), with both low-wavenumber tomographic and high-resolution detailed updates.
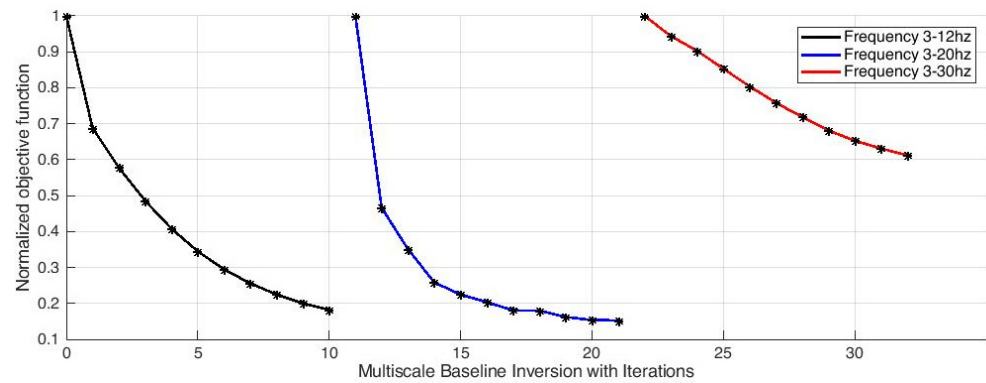
Figure 9. Convergence curves of 3D multi-scale elastic-waveform inversion of the baseline VSP data at three frequency scales.
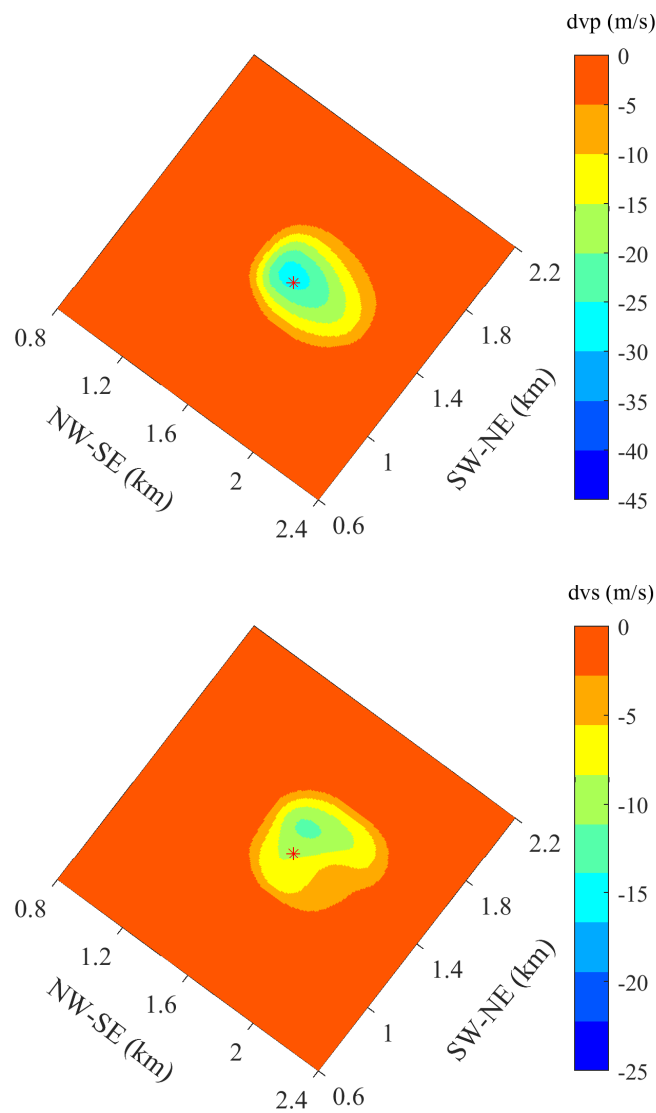
Figure 10. Inverted time-lapse velocity changes between baseline and Monitor 1 VSP surveys at the center depth of Morrow B. The red asterisk labels the VSP/injection-well position.
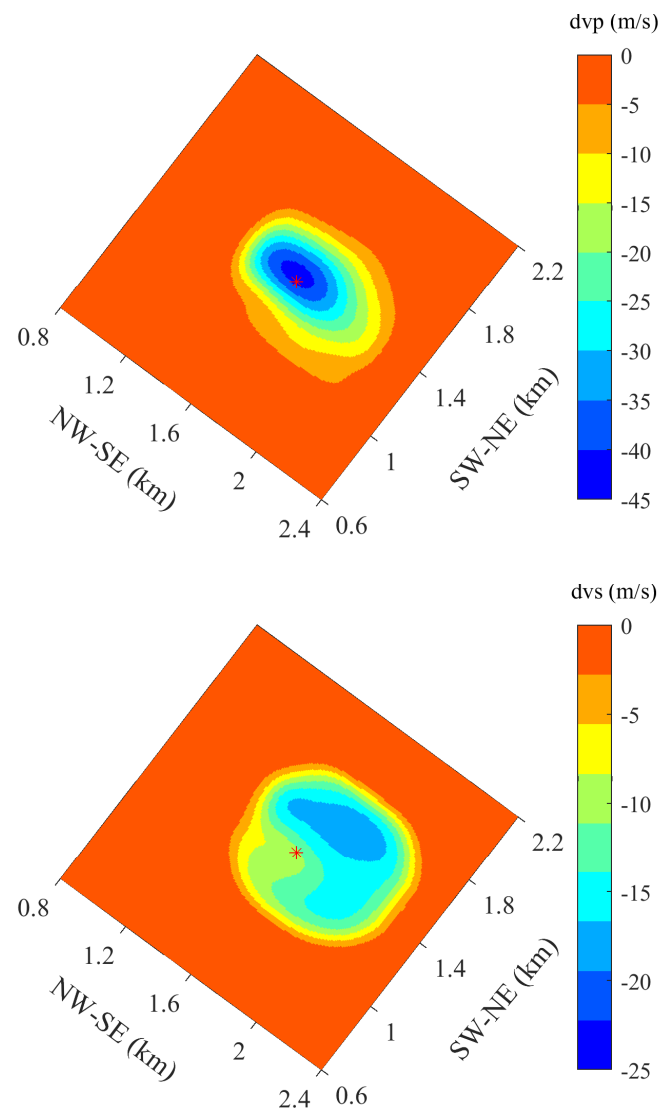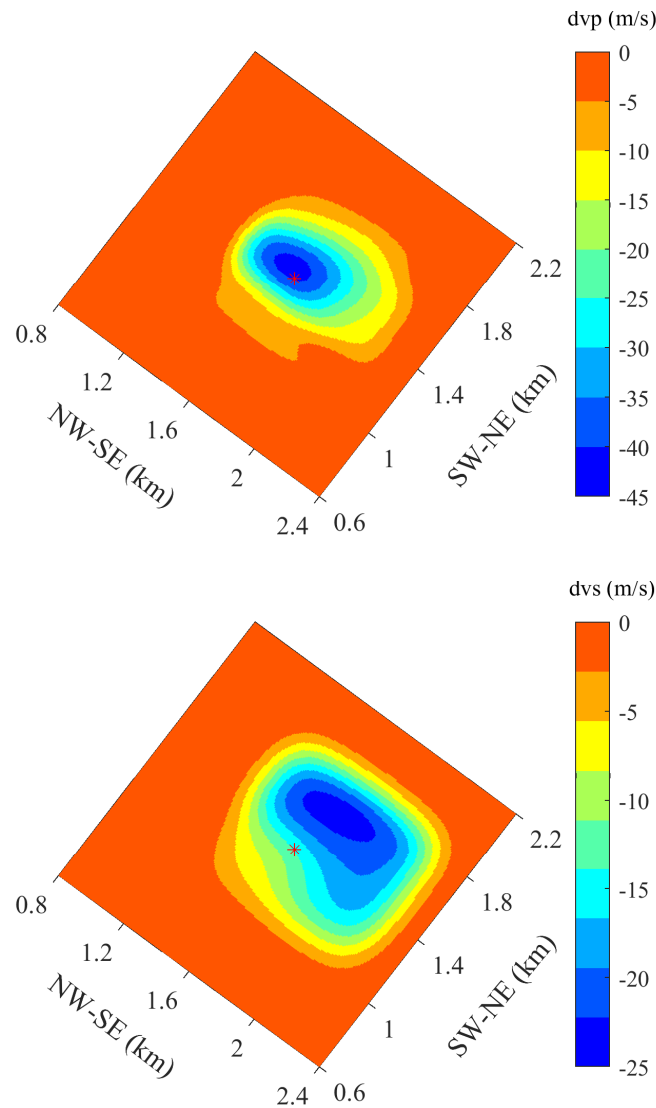
Figure 11. Inverted time-lapse velocity changes between baseline and Monitor 2 VSP surveys at the center depth of Morrow B. The red asterisk labels the VSP/injection-well position.

We plot the volumetric contour of our inverted velocity changes to visualize the spatiotemporal evolution of the CO_2 plume. We plot the velocity contours of -5 m/s, as shown in Figures 15–17; these figures vividly display the evolution of the CO_2 plume between baseline and Monitor 1, between baseline and Monitor 2, and between baseline and Monitor 3, respectively. They show how the CO_2 plume drives the oil and gas from the CO_2 injection well to the oil/gas production wells.

The results in Figures 10–12 and 15–17 show that the relative changes of increasing velocity reductions and increasing CO_2 plume volume among time-lapse seismic surveys are reliably inverted. The sequential inversion strategy allows the time-lapse inversion stage to focus on the velocity changes and decreases the possible influence of the baseline velocity errors. However, absolute values of velocity changes may still not be very accurate and may contain some uncertainties. According to the above rock-physics analysis, the inverted V_p and V_s changes are smaller than expected. In field data applications, data noise, limited angle coverage in the subsurface, wavefield propagation in real Earth media (such as anisotropy and attenuation), and inversion algorithms and parameters used in inversion all influence the absolute values of the inverted velocity changes. For example, of the lack of anisotropy parameters results in the estimated velocity changes are equivalent values attributing anisotropic factors into velocity values. On the other hand, the results

in Figures 10–12 and the 1D comparison in Figure 14 show that the resolution of V_p and V_s changes are about dozens of meters; Figure 14 also suggests that V_s changes have higher spatial resolution than V_p changes. Nevertheless, inverted time-lapse V_p and V_s changes successfully reveal the migration of the CO_2 plume from the injection well to the production well.

Figure 12. Inverted time-lapse velocity changes between baseline and Monitor 3 VSP surveys at the center depth of Morrow B. The red asterisk labels the VSP/injection-well position.
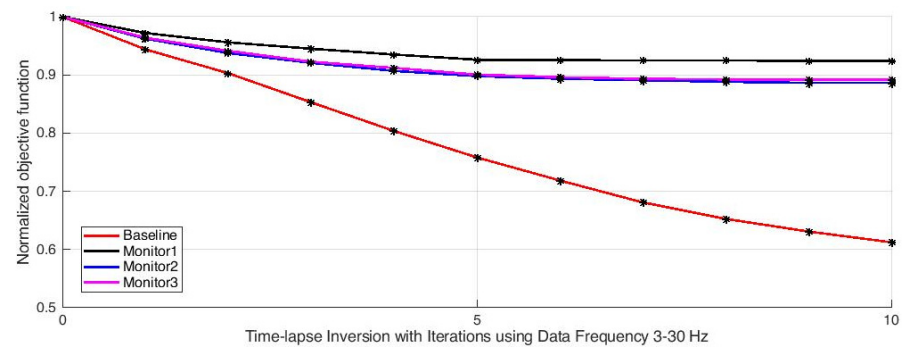
Figure 13. Comparison of convergence curves of baseline and three monitoring datasets at the final frequency scale.
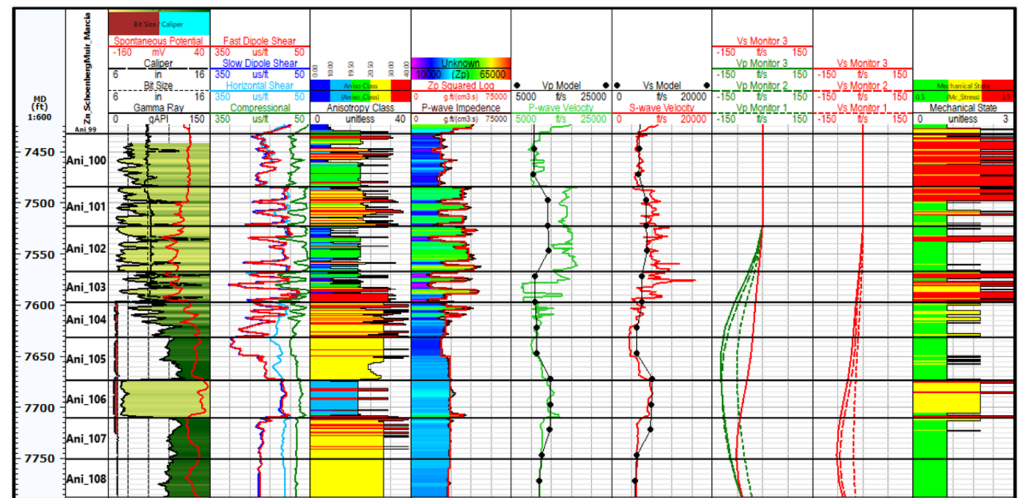
Figure 14. Results of the time-lapse VSP inversion in relation to the Mechanical Earth Model (MEM). Track 1 shows the measured depth, track 2 shows the layers used for the upscaling of the log data to the VSP scale, track 3 shows the correlation curves, track 4 shows the dipole acoustical slownesses, track 5 shows the anisotropy classification, track 6 shows the P-wave impedance used to define the layers, track 7 shows the upscaled V_p model in black and the P-wave log velocity in green, track 8 shows the upscaled V_s model in black and the S-wave log velocity in red, track 9 shows the change in P-wave velocity for the three monitor surveys in green and the third time-lapse S-wave monitor in red, track 10 shows the change in S-wave velocity for the three monitor surveys in red, and track 11 shows the mechanical behavior. Here the depth unit is feet (0.3048 m) and velocity unit is feet/s (0.3048 m/s).
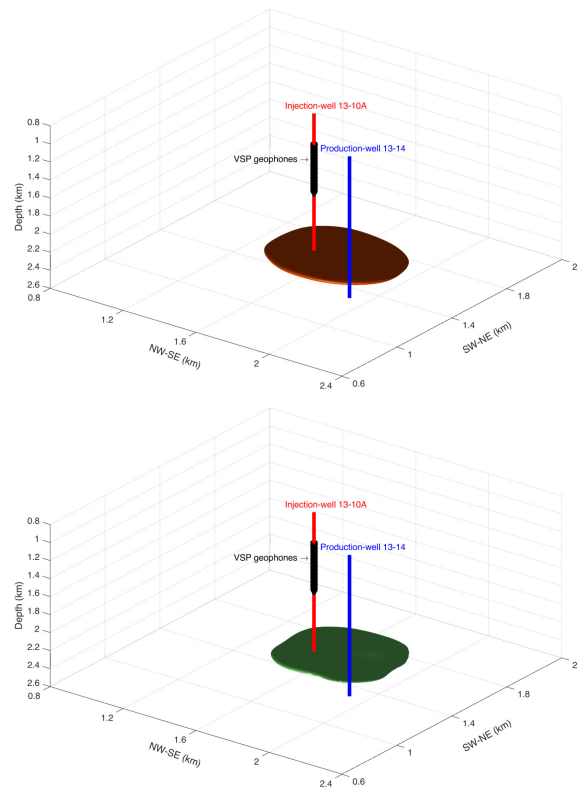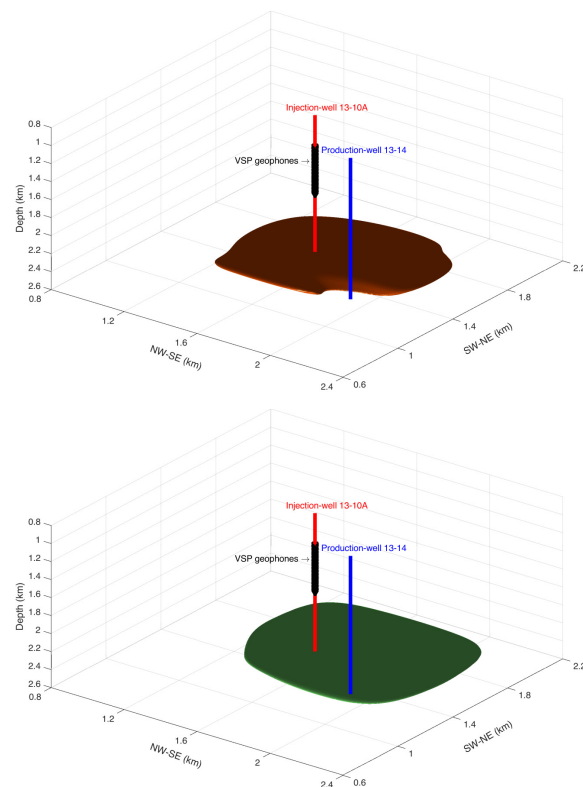

Figure 15. The volumetric contours of inverted time-lapse velocity changes between baseline and Monitor 1 VSP surveys, where brown and green colors indicate V_p and V_s changes, respectively.
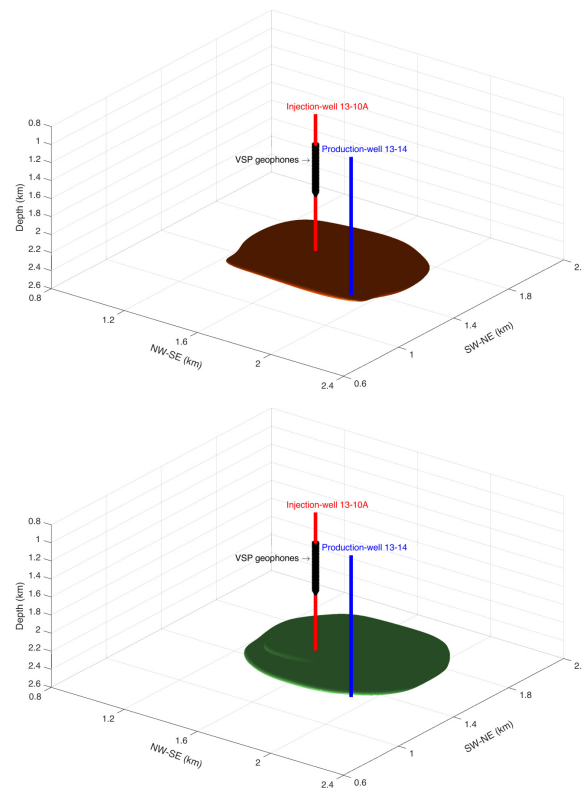
Figure 16. The volumetric contours of inverted time-lapse velocity changes between baseline and Monitor 2 VSP surveys, where brown and green colors indicate V_p and V_s changes, respectively.

Figure 17. The volumetric contours of inverted time-lapse velocity changes between baseline and Monitor 3 VSP surveys, where brown and green colors indicate V_p and V_s changes, respectively.

5. Conclusions

We have performed 3D elastic-waveform inversion of the time-lapse 3D-3C VSP data acquired at the Farnsworth CO_2-EOR field to monitor the spatiotemporal evolution of the CO_2 plume. We have built baseline velocity models for time-lapse inversion using sonic logs, the velocity model derived from the 3D surface seismic data, 3D tomography of first arrivals of the baseline VSP downgoing waves, and elastic-waveform inversion of the upgoing waves of the baseline VSP data. We employ the spatial prior information in elastic-waveform inversion of time-lapse 3D-3C VSP data to improve the inversion robustness. Our results of time-lapse elastic-waveform inversion show the decreasing time-lapse velocities with the increasing of CO_2 injection; these are validated through comparison with borehole sonic logging and petrophysical prior information. The volumetric contour plots of the time-lapse velocity changes reveal the spatiotemporal evolution of the CO_2 plume, driving oil and gas from the CO_2 injection well to the oil/gas production wells.

Conflicts of Interest: The authors declare no conflict of interest.

References

1. Lumley, D.; Adams, D.C.; Meadows, M.; Cole, S.; Wright, R. 4D seismic data processing issues and examples. In Proceedings of the 73rd Annual International Meeting, SEG, Expanded Abstracts, Dallas, TX, USA, 26–31 October 2003; pp. 1394–1397.
2. Huang, L. *Geophysical Monitoring for Geologic Carbon Storage*; AGU-Wiley Monograph; John Wiley & Sons: Hoboken, NJ, USA, 2022.
3. Ajo-Franklin, J.B.; Minsley, B.J.; Daley, T.M. Applying compactness constraints to differential traveltime tomography. *Geophysics* **2007**, *72*, R67–R75. [CrossRef]
4. Daley, T.M.; Myer, L.; Peterson, J.E.; Majer, E.L.; Hoversten, G.M. Time-lapse crosswell seismic and VSP monitoring of injected CO_2 in a brine aquifer. *Environ. Geol.* **2008**, *54*, 1657–1665. [CrossRef]
5. Zhang, Z.; Huang, L. Double-difference elastic-waveform inversion with prior information for time-lapse monitoring. *Geophysics* **2013**, *78*, R259–R273. [CrossRef]
6. Virieux, J.; Operto, S. An overview of full-waveform inversion in exploration geophysics. *Geophysics* **2009**, *74*, WCC1–WCC26. [CrossRef]
7. Asnaashari, A.; Brossier, R.; Garambois, S.; Audebert, F.; Thore, P.; Virieux, J. Time-lapse seismic imaging using regularized full-wave-form inversion with a prior model: Which strategy? *Geophys. Prospect.* **2015**, *63*, 78–98. [CrossRef]
8. Raknes, E.B.; Arntsen, B. A numerical study of 3D elastic time-lapse full-waveform inversion using multicomponent seismic data. *Geophysics* **2015**, *80*, R303–R315. [CrossRef]
9. Egorov, A.; Pevzner, R.; Bóna, A.; Glubokovskikh, S.; Puzyrev, V.; Tertysh-nikov, K.; Gurevich, B. Time-lapse full-waveform inversion of vertical seismic profile data: Workflow and application to the CO2CRC Otway project. *Geophys. Res. Lett.* **2017**, *44*, 7211–7218. [CrossRef]
10. Kamei, R.; Lumley, D. Full waveform inversion of repeating seismic events to estimate time-lapse velocity changes. *Geophys. J. Int.* **2017**, *209*, 1239–1264. [CrossRef]
11. Liu, X.; Zhu, T.; Ajo-Franklin, J. Understanding Subsurface Fracture Evolution Dynamics Using Time-Lapse Full Waveform Inversion of Continuous Active-Source Seismic Monitoring Data. *Geophys. Res. Lett.* **2023**, *50*, e2022GL101739. [CrossRef]

12. Li, Q.; Wang, F.; Wang, Y.; Zhou, C.; Chen, J.; Forson, K.; Miao, R.; Su, Y.; Zhang, J. Effect of reservoir characteristics and chemicals on filtration property of water-based drilling fluid in unconventional reservoir and mechanism disclosure. *Environ. Sci. Pollut. Res.* **2023**, *30*, 55034–55043. [CrossRef] [PubMed]

13. Liu, X.; Huang, L.; Feng, Z.; El-Kaseeh, G.; Will, R.; Balch, R. Efficient 3-D velocity model building using joint inline and crossline plane-wave wave-equation migration velocity analyses. *Geophys. J. Int.* **2021**, *225*, 37–53. [CrossRef]

14. Liu, X.; Liu, Y.; Khan, M. Fast least-squares reverse time migrationof VSP free-surface multiples with dynamic phase-encoding schemes. *Geophysics* **2018**, *83*, S321–S332. [CrossRef]

15. Carcione, J.; Picotti, S.; Cavallini, F.; Santos, J. Numerical test of the Schoenberg-Muir theory. *Geophysics* **2012**, *77*, C27–C35. [CrossRef]

16. Woodward, M.J.; Nichols, D.; Zdraveva, O.; Whitfield, P.; Johns, T. A decade of tomography. *Geophysics* **2008**, *73*, VE5–VE11. [CrossRef]

17. Taillander, C.; Noble, M.; Chauris, H.; Calandra, H. First-arrival traveltime tomography based on the adjoint-state method. *Geophysics* **2009**, *74*, WCB1–WCB10. [CrossRef]

18. Routh, P.; Krebs, J.; Lazaratos, S.; Baumstein, A.; Lee, S.; Cha, Y.H.; Downey, N.; Hinkley, D.; Anderson, J. Encoded simultaneous source full wavefield inversion for spectrally shaped marine streamer data. In Proceedings of the 81st Annual International Meeting, SEG, Expanded Abstracts, San Antonio, TX, USA, 18–23 September 2011; pp. 2433–2438.

19. Fei, T.W.; Luo, Y.; Yang, J.; Liu, H.; Qin, F. Removing false images in reverse time migration: The concept of de-priming. *Geophysics* **2015**, *80*, S237–S244. [CrossRef]

20. Chi, B.; Gao, K.; Huang, L. Least-squares reverse time migration guided full-waveform inversion. In Proceedings of the 87th Annual International Meeting, SEG, Expanded Abstracts, Houston, TX, USA, 24–29 September 2017; pp. 1471–1475.

21. Gao, K.; Huang, L. Acoustic- and elastic-waveform inversion with total generalized p-variation regularization. *Geophys. J. Int.* **2019**, *218*, 933–957. [CrossRef]

22. Czoski, P. Geologic Characterization of the Morrow B Reservoir in Farnsworth Unit, TX Using 3D VSP Seismic, Seismic Attributes, and Well Logs. Master's Thesis, New Mexico Tech, Socorro, NM, USA, 2014.

23. Rickett, J.; Lumley, D.E. Cross-equalization data processing for time-lapse seismic reservoir monitoring: A case study from the Gulf of Mexico. *Geophysics* **2001**, *66*, 1015–1025. [CrossRef]

24. Wang, Z.; Cates, M.E.; Langan, R.T. Seismic monitoring of a CO_2 flood in a carbonate reservoir: A rock physics study. *Geophysics* **1998**, *63*, 1604–1617. [CrossRef]